Heterogeneous & Homogeneous & Bio-
CHEMCATCHEM
CATALYSIS

Supporting Information

Assessment of the 3D Pore Structure and Individual Components of Preshaped Catalyst Bodies by X-Ray Imaging

Julio C. da Silva,*[a] Kevin Mader,[a] Mirko Holler,[a] David Haberthür,[a] Ana Diaz,[a] Manuel Guizar-Sicairos,[a] Wu-Cheng Cheng,[b] Yuying Shu,[b] Jörg Raabe,[a] Andreas Menzel,[a] and Jeroen A. van Bokhoven*[a, c]

cctc_201402925_sm_miscellaneous_information.pdf
cctc_201402925_sm_movie_s1.mpg

Supporting Information on Experiment and Methods

Sample Preparation for X-ray imaging experiments:

The sample was a composite Fluid Catalytic Cracking (FCC) catalyst formed by metakaolin (calcined kaolin clay) and zeolite type Y with about 5% La_2O_3 exchange. They form spherical bodies with diameter of about 100 µm as shown in Figure SI-1. For microtomography experiments, the powder containing the catalyst bodies was put inside a quartz capillary, and no further preparation was carried out before the experiments. For the ptychographic X-ray nanotomography experiments, the sample was milled using FIB to extract a cylinder of 8 µm diameter out of one spherical catalyst body as shown in Figure SI-1. This cylinder was mounted on the sample holder of the instrument[S1,S2] as shown in Figure SI-1d.

X-ray microtomography experiments:

Microtomography experiments were performed at the TOMCAT beamline[S3] at the Swiss Light Source, Paul Scherrer Institut, Switzerland. The sample was measured with a parallel X-ray beam geometry at a photon energy of 20 keV. Using a propagation-based phase contrast approach, the contrast between phase differences in the sample was enhanced at a single propagation distance of 15 mm.[S4,S5] For using Paganin's approach for phase retrieval[S6] of the projections an assumption of the complex-valued index of refraction $n(\mathbf{r}) = 1 - \delta(\mathbf{r}) + i\,\beta(\mathbf{r})$ is required. We used an estimate for the ratio δ/β of 478, based on the known properties of aluminum silicate. This allowed obtaining a reasonably good contrast in the images although the quantitative information in the gray level is lost. For the detection system, the X-rays were converted to visible light by a 20 µm thick LAG:CE scintillator (Crytur Ltd., Turnov, Czech Republic) and magnified by an optical microscope (Optique Peter, Lentilly, France), which results in an isometric voxel size of 0.33 µm. 1501 projections were recorded with a field of view of 2560 × 2160 pixels over a rotation of 180º. 32 dark-field and 100 flat-field images were also acquired for correction of the detector noise and flat-field. The exposure time of each projection was 220 ms and the whole scan took 7 min and 40 s. These 2D projections were used for the tomographic reconstruction as described by Marone *et al.*[S7] The X-ray dose imparted to the specimen was approximately 6×10^4 Gy, calculated according to Lovric *et al.*[S8] based on the given experimental parameters. The total size of the tomogram was 2560 × 2560 × 2160 voxels. The 3D renderings shown in Figure 1 of the main text were done with three-dimensional datasets cropped to the volume of the capillary. The tomographic dataset were visualized in MeVisLab (version 2.5.1, 2013-11-21 Release).

Ptychographic X-ray nanotomography experiments:

Ptychographic X-ray nanotomography experiments were carried out at the cSAXS beamline at the Swiss Light Source, Paul Scherrer Institut, Switzerland. The X-rays were produced by an U19 undulator and the photon energy was set at 6.2 keV (wavelength of 2Å) by using a double-crystal Si(111) monochromator. The horizontal aperture of the slits located at about 22 m upstream the sample and close to the undulator was set to 20 µm to increase the transverse coherence of the X-ray beam which is originally 25 × 250 μm^2 horizontal × vertical FWHM at the plane of the sample. The coherent illumination onto the sample was defined by a gold Fresnel zone plate (FZP) whose diameter was 170 µm and outermost zone width was of 60 nm.[S9] The sample was placed 0.5 mm downstream of the FZP focal point resulting in an illumination probe size at the sample of about 1.6 µm. Coherent diffraction patterns were acquired using a PILATUS detector[S10,S11] with pixel size of 172 µm and placed 7.36 m downstream of the sample. A 2 × 2 binning of the detector pixels was performed to speed up the calculations. A He-flushed tube was positioned between the sample and the detector to reduce air scattering and absorption. The measurements were carried out using the instrumentation described by Holler *et al.*[S1,S2] The projections were acquired using a binary acquisition strategy described by Kaestner *et al.* with 8 nests of projections.[S12] 450 projections were acquired with angular step of 0.4º. Each projection was obtained by a ptychographic scan of 419 diffraction patterns with an exposure time of 0.1 seconds each, which were collected in about 142 seconds for each projection, including the time needed for sample positioning and detector readout. The field of view covered in each projection was of 13 × 10 μm^2 (horizontal × vertical). The X-ray dose imparted to the specimen was 2×10^8 Gy, estimated based on the number of photons absorbed by the sample (integration of all diffraction patterns) multiplied by the photon energy and divided by sample mass estimated from the tomogram. In order to avoid a pathology which can be caused by a periodic scan grid[S13], the sampling positions lay on circular shells with a radial step size of 0.5 µm and with 5 equally spaced points in the first inner shell. To compensate the lost information due to the gaps between PILATUS detector modules, after each two successive projections the detector was moved perpendicular to the propagation direction of the X-ray by the same amount of gap sizes vertically and horizontally as described in previous works.[S2,S14,S15] The ptychographic scan in each tomographic angle was performed only once, and the detector position was alternated every two successive scans.

From each diffraction pattern, a region of 600 × 600 pixels was used in the reconstructions, resulting in a pixel size of 14.3 nm in the reconstructed projections. Each reconstruction was obtained with 200 iterations of the difference map algorithm[S16] followed by 100 iterations of likelihood refinement.[S17,S18] These reconstructions were performed by sharing information on the illumination between consecutive scans taken at different projection angles. This way, the intensities within the detector gaps are sufficiently constrained.[S2,S14,S15] Prior to the tomography reconstructions, the complex-valued projections were processed and aligned according to Guizar-Sicairos *et al.*[S19] The tomographic reconstruction was performed on the phase projections using a modified filtered backprojection algorithm (FBP) suitable for wrapped phase.[S18] To mitigate noise in the reconstruction, a Hanning filter was used with 1.0 normalized cut-off frequency. The resulting tomogram provides the 3D distribution of the refractive index decrement, $\delta(\mathbf{r})$, and away from absorbing edges, it provides the electron density.[S20,S21] After the image segmentation of the material phases, the mass density of each component of the sample was estimated as described by Diaz *et al.*[S21] For the mass density estimation, the ratio of molar mass and number of electrons of the material was approximated to 2, which is a fairly good approximation for light elements with the exception of Hydrogen and which has been used in other works in the literature.[S22-S24] Usually, one can expect a systematic error of about 10 % in the estimates using this approximation. Therefore, although the relative statistical errors of our estimates of mass density were less than 1%, we assumed the systematic plus statistical relative errors as 10%, which was considered as the relative error of the measurements.

Estimation of the spatial resolution of the X-ray images:

The spatial resolution of the 3D X-ray images was estimated by different approaches for each technique. For the phase contrast microtomography, the resolution was estimated by Fourier Ring Correlation (FRC)[S25] on different axis slices, whereas for the ptychographic X-ray tomography, this was done by Fourier shell correlation (FSC) [S26] on the reconstructed volume. In the former, the Fourier correlation is done for some randomly chosen 2D slices of the tomogram and the curves are averaged, while in the latter the Fourier correlation is calculated in 3D using a region of the tomogram. In both cases, the full dataset of projections used for the tomography reconstruction was divided in half and two independent tomograms with double angular spacing were reconstructed independently. Then, a correlation curve in Fourier domain is obtained between the two tomograms and the resolution is estimated dividing the voxel size by the abscissa value at its intersection with a threshold curve.[S2, S25-S27] The threshold criteria for FRC was the 2-σ criterion and for FSC we are using the ½ bit criteria, which is more stringent. Although different, we do not expected much differences in the resolution estimation which could compromise the results here presented. Figure SI-2 shows the results.

Segmentation of the material phases from the 3D images:

A threshold-based segmentation of the 3D images obtained with ptychographic X-ray nanotomography experiment was performed to separate the pores from the material, followed by image processing morphological operations to refine the segmentation.[S28] The high signal-to-noise ratio of the 3D images allowed separating the components of the FCC catalyst based on the intensity threshold. From the gray-intensity histogram, we chose a threshold placed midway between the two peaks of the two materials. Then, we recalculated the gray-intensity histogram for each of the components and used them to assist the refinement the images with morphological operators (opening and closing operators).[S28] Afterwards, the materials phases were identified and the segmentation was performed by selecting the proper range of $\delta(\mathbf{r})$ corresponding to each phase on the phase contrast images. Then, an average value of $\delta(\mathbf{r})$ of each phase was calculated and the corresponding mass density was estimated as described above, which complemented the identification of the material phases and was subsequently confirmed by the shapes of the materials components within the FCC catalyst structure. The mass density sensitivity and spatial resolution of the 3D image we obtained by ptychographic X-ray tomography allows unambiguous identification of these materials without further need for additional experiments. Once the two components were segmented, the pores were segmented by considering the regions not occupied by the materials, excluding the regions external to the sample, which also contains air. This provided a mask for each of the material components and another one for the pores. These segmentation procedures and all the 3D renderings were carried out using the commercial Avizo® Fire software.

Pore size analysis from the 3D images:

The pores were analyzed using neighborhood-based component labeling to identify contiguous pore regions. Each of these labeled regions was analyzed in shape, connectivity, and distribution.[S29] Since many of the pore spaces were physically connected, a thickness analysis was performed to identify the unique pore spaces and their radii, which was multiplied by 2 for pore diameter to be comparable to other measures. This method transforms the segmented image into a map where the gray intensity in each voxel in the porosity regions is replaced by the radius of the largest sphere, which can entirely fit into the porous region surrounding the voxel.[S30] In such a way, a pore radius map is created, which is subsequently used to obtain the distribution of pore sizes independent of any additional model constraints. Since the analysis is based on the largest sphere which fits in any given region, non-spherical structures and particularly rough surfaces will lead to higher counts for very small spheres (which are the largest objects that fit in a rough region) as observed in the pore size distribution of figure 3a from the main text. The smaller spheres with radii of several pixel lengths can then be ignored when making the comparison.[S30]

Mercury Porosimetry:

The mercury PSD measurement was carried out on a Micromeritics Autopore IV 9520 unit. The sample was pre-treated at 200ºC for 15 minutes, then at 540ºC for 1 hour. 0.35 grams of the sample was loaded into a 3 cc powder penetrometer. The mercury intrusion pressure was increased in a stepwise manner from 0.1 to 60,000 psi. The volume of mercury intruded after each step is measured and recorded. The pore diameter is calculated using the Washburn equation with a contact angle of 140 degrees.[S31]

Links to access the tomographic datasets:

The slices of the tomograms obtained by phase contrast microtomography and ptychographic nanotomography are available in the links below, along with the thickness maps created for the pore size analysis.

Dataset from X-ray ptychographic nanotomography experiments:
- Some axial slices of the tomogram in grayscale: http://people.ee.ethz.ch/~maderk/dz/csaxs.html
- Some axial slices of the tomogram In Color: http://people.ee.ethz.ch/~maderk/dz/csaxs_rgb.html
- The resulting thickness maps from the thickness analysis for pore size estimation: http://people.ee.ethz.ch/~maderk/dz/csaxs_dto.html

Dataset from X-ray phase contrast microtomography experiments:
- Some axial slices of the tomogram In grayscale: http://people.ee.ethz.ch/~maderk/dz/tomcat.html
- The resulting thickness maps from the thickness analysis for pore size estimation: http://people.ee.ethz.ch/~maderk/dz/tomcat_dto.html

Supporting Information Video

Movie1.mpg
Video SI-1 – 3D rendering of the ptychographic X-ray nanotomography data. In the first part of the movie, the material is shown in bright yellow and the interparticle space is shown in orange. In the second part, the zeolites are shown in blue and the metakaolin clay in red.

Supporting Information References

[S1] M. Holler, J. Raabe, A. Diaz, M. Guizar-Sicairos, C. Quitmann, A. Menzel, O. Bunk, *Rev. Sci. Instrum.* **2012**, *83*, 073703.

[S2] M. Holler, A. Diaz, M. Guizar-Sicairos, P. Karvinen, E. Färm, E. Härkönen, M. Ritala, A. Menzel, J. Raabe, O. Bunk, *Sci. Rep.* **2014**, *4*, 3857.

[S3] M. Stampanoni, A. Groso, A. Isenegger, G. Mikuljan, Q. Chen, A. Bertrand, S. Henein, R. Betemps, U. Frommherz, P. Böhler, D. Meister, M. Lange, R. Abela. In: *Proceedings of SPIE*. Ed. by Ulrich Bonse. Vol. 6318. Society of Photo-Optical Instrumentation Engineers (SPIE) Conference Series. SPIE, Aug. **2006**.

[S4] A. Snigirev, I. Snigireva, V. Kohn, S. Kuznetsov, I. Schelokov, *Rev. Sci. Instrum.* **1995**, *66*, 5486.

[S5] P. Cloetens, W. Ludwig, J. Baruchel, J.-P. Guigay, P. Pernot-Rejmánková, M. Salomé-Pateyron, M. Schlenker, J.-Y. Buffière, E. Maire, G. Peix, *J. Phys. D: Appl. Phys.* **1999**, *32*, A145-A151.

[S6] D. Paganin, S. C. Mayo, T. E. Gureyev, P. R. Miller, S. W. Wilkins, *J. Microsc.* **2002**, *206*, 33-40.

[S7] F. Marone, M. Stampanoni, *J. Synchrotron Rad.* **2012**, *19*, 1029-1037.

[S8] G. Lovric, S. F. Barré, J. C. Schittny, M. Roth-Kleiner, M. Stampanoni, R. Mosko, *J. Appl. Cryst.* **2013**, *46*, 856-860.

[S9] S. Gorelick, J. Vila-Comamala, V. A. Guzenko, R. Barrett, M. Salome, C. David, *J. Synchrotron Rad.* **2011**, *18*, 442-446.

[S10] B. Henrich, A. Bergamaschi, C. Bronnimann, R. Dinapoli, E. F. Eikenberry, I. Johnson, M. Kobas, P. Kraft, A. Mozzanica, B. Schmitt, *Nucl. Instrum. Meth. Phys. Res. A* **2009**, *607*, 247-249.

[S11] P. Kraft, A. Bergamaschi, C. Bronnimann, R. Dinapoli, E. F. Eikenberry, H. Graafsma, B. Henrich, I. Johnson, M. Kobas, A. Mozzanica, C. M. Schleputz, B. Schmitt, *IEEE T. Nucl. Sci.* **2009**, *56*, 758-764.

[S12] A. Kaestner, B. Munch, P. Tritk, L. Butler, *Opt. Eng.* **2011**, *50*, 123201.

[S13] P. Thibault, M. Dierolf, O. Bunk, A. Menzel, F. Pfeiffer, *Ultramicroscopy* **2009**, *109*, 338-343.

[S14] I. Zanette, *Ptychographic reconstructions using shared data sets. Paper presented at Coherence: International Workshop on Phase Retrieval and Coherent Scattering*, Japan. Place of publication: Hilton Fukuoda Sea Hawks, Fukuoka, Japan; Manuscript in preparation by M. Dierolf, **2012**.

[S15] M. Guizar-Sicairos, I. Johnson, A. Diaz, M. Holler, P. Karvinen, H.-C. Stadler, R. Dinapoli, O. Bunk, A. Menzel, *Opt. Express* **2014**, *22*, 14859-14870.

[S16] P. Thibault, M. Dierolf, A. Menzel, O. Bunk, C. David, F. Pfeiffer, *Science* **2008**, *321*, 379-382.

[S17] M. Guizar-Sicairos, J. R. Fienup, *Opt. Express* **2008**, *16*, 7264-7278.

[S18] P. Thibault, M. Guizar-Sicairos, *New J. Phys.* **2012**, *14*, 063004.

[S19] M. Guizar-Sicairos, A. Diaz, M. Holler, M. S. Lucas, A. Menzel, R. A. Wepf, O. Bunk, *Opt. Express* **2011**, *19*, 21345-21357.

[S20] M. Dierolf, A. Menzel, P. Thibault, P. Schneider, C. M. Kewish, R. Wepf, O. Bunk, F. Pfeiffer, *Nature* **2010**, *467*, 436-439.

[S21] A. Diaz, P. Trtik, M. Guizar-Sicairos, A. Menzel, P. Thibault, O. Bunk, *Phys. Rev. B* **2012**, *85*, 020104(R).

[S22] A. Diaz, M. Guizar-Sicairos, A. Poeppel, A. Menzel, O. Bunk, *Carbon* **2014**, *67*, 98-103.

[S23] A. Guinier, *X-Ray Diffraction In Crystals, Imperfect Crystals, and Amorphous Bodies*, Dover Publications Inc., New-York, **1994**.

[S24] M. Langer, A. Pacureanu, H. Suhonen, Q. Grimal, P. Cloetens, F. Peyrin, *PLoS ONE* **2012**, *7*, e35691.

[S25] N. Banterle, K. H. Bui, E. A. Lemke, M. Beck, *J. Struct. Biol.* **2013**, *183*, 363-367.

[S26] M. van Heel, M. Schatz, *J. Struct. Biol.* **2005**, *151*, 250-262.

[S27] J. Vila-Comamala, A. Diaz, M. Guizar-Sicairos, A. Mantion, C. M. Kewish, A. Menzel, O. Bunk, C. David, *Opt. Express* **2011**, *19*, 21333-21344.

[S28] R. C. Gonzalez, R. E. Woods, *Digital Image Processing*, 3rd edition, Prentice-Hall, Upper Saddle River, NJ, USA, **2008**.

[S29] K. S. Mader, P. Schneider, R. Müller, M. Stampanoni. *Bone* **2013**, *57*, 142–154.

[S30] T. Hildebrand, P. Ruegsegger, *J. Microsc.* **1997**, *185*, 67-75.

[S31] E. W. Washburn, *Phys. Rev.* **1921**, *17*, 273-283.

Supporting Information Figures

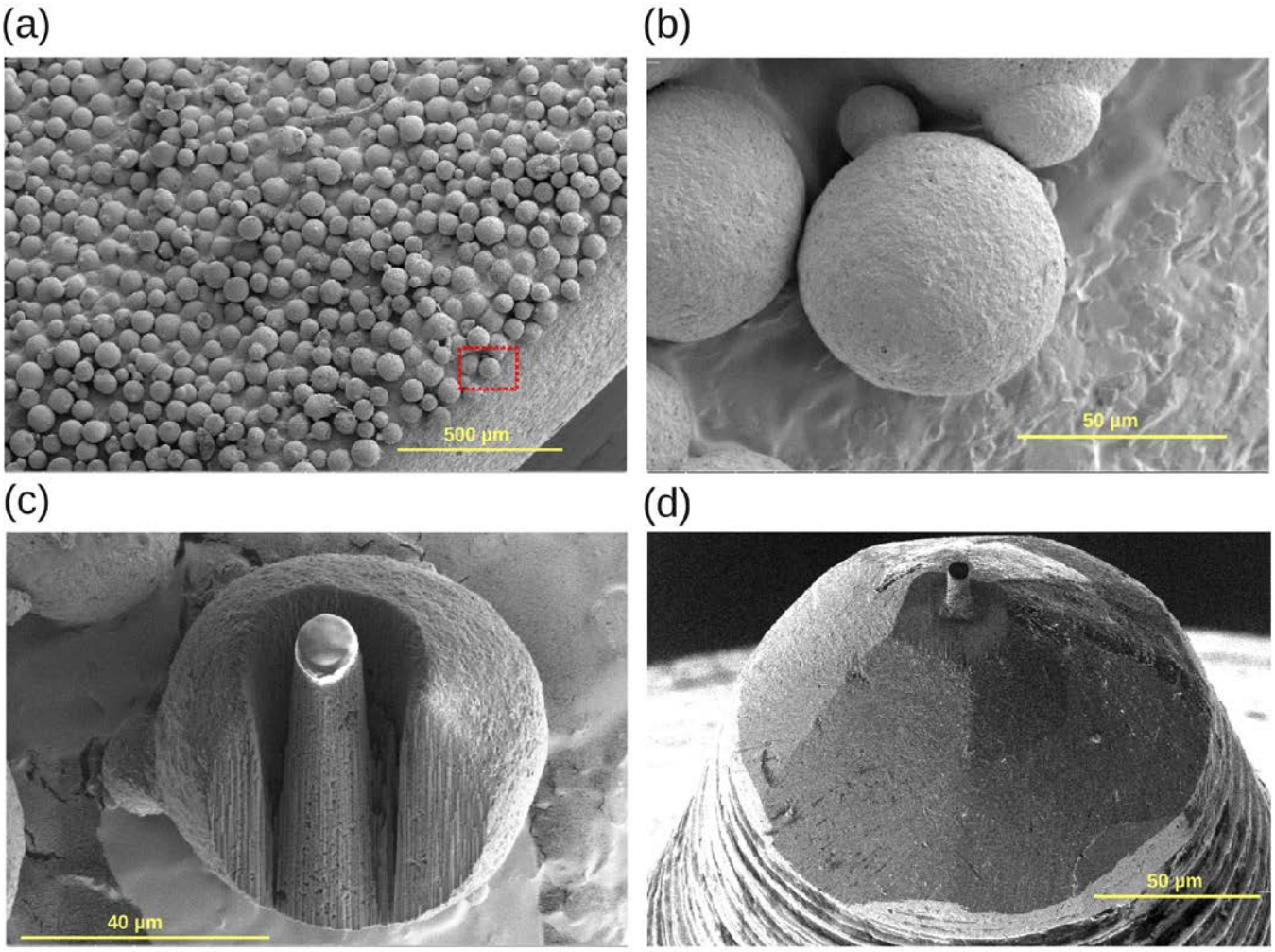

Figure SI-1– SEM images and focused ion beam milling sample preparation. **(a)** SEM of the spherical catalyst bodies of sample. The dashed red line square indicates the zoomed-in are presented in (b). **(b)** Zoom-in of one particle. **(c)** Focused ion beam milling of sample pillar. **(d)** Milled pillar mounted on the sample holder.

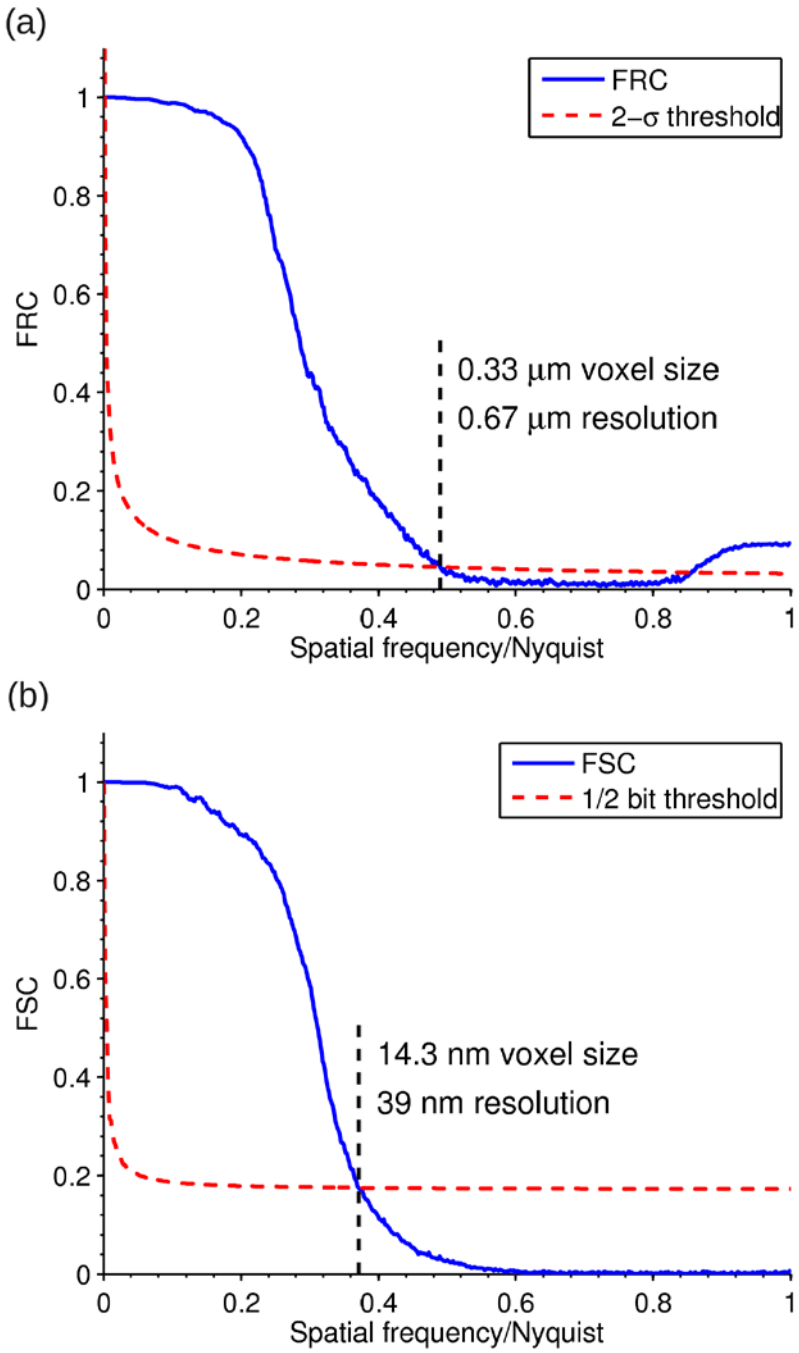

Figure SI-2 – Estimation of spatial resolution images from the tomograms of the FCC catalyst body. **(a)** The resolution estimate from the microtomography results using Fourier Ring Correlation (FRC) in some randomly selected 2D slices of the tomogram. **(b)** The resolution estimate from the nanotomography results using 3D Fourier Shell Correlation (FSC) in a region of the tomogram. The half-period resolution and the voxel size are indicated on the plot for the crossing points of the Fourier correlation curve in blue and the threshold curve in dashed red line. These values are obtained by dividing the pixel size by the abscissa value at the intersection point of the two curves.